ADVANCED ENGINEERING MATERIALS
www.aem-journal.com

Enhancing Fatigue Performance by Tuning of Residual Stresses in Welded Joints through Nanometallic Multilayer

Niclas Spalek, Guilherme Abreu Faria, Anton Davydok, and Marcus Rutner*

Welded joints suffer from reduced fatigue life due to geometric stress concentrations and metallurgical changes in the heat-affected zone that promote crack initiation under cyclic loading. This study investigates a novel postweld treatment, utilizing a Cu/Ni nanometallic multilayer thin film deposited onto the welded butt joint. Deposition current densities and individual Cu/Ni layer thicknesses are systematically varied to optimize fatigue performance. A multiscale residual stress (RS) analysis characterizes stress states within individual multilayers and in the steel substrate, indicating all substrate RS are compressive in nature after thin film deposition. Results demonstrate a direct correlation between compressive RS magnitude and fatigue strength improvement. Tested at $\Delta\sigma_R = 0.75 \times f_y$, a more than a 300% increase in cycles to failure is seen compared to the as-welded condition. This postweld treatment offers a promising approach for extending the operational life of welded structures across industrial applications.

1. Introduction

The integrity and longevity of welded structures are of principal importance across industries, ranging from automotive to construction and marine engineering. Fatigue and corrosion are the most prominent reasons for premature failure of engineering products. As a result, increasing the usable lifetime of structures directly impacts sustainable use and materials consumption. Considering that 40% of the annual global steel demand is allocated to replacing products that have reached the end of their lifetime or failed prematurely,[1] it is evident that extending the usable lifespan of infrastructure offers a significant opportunity to reduce carbon oxide emissions.

Welding, while a fundamental joining technique, inevitably introduces residual stresses (RS) and microstructural changes that can compromise the performance and durability of welded components. Among all engineering products, more than half contain welded connections.[2] In the context of structural longevity, cyclic loading is especially critical for welded joints, as profile changes in the weld toe can introduce stress concentrations. Additionally, rapid heating and subsequent cooling is responsible for localized phase transformations, grain growth and impeded shrinkage in the heat-affected zone (HAZ) contributing to an impaired fatigue strength.[3–5] In order to constrain these effects on the fatigue strength, so-called postweld treatments are developed. According to the International Institute of Welding (IIW), postweld treatments can be categorized into three groups. Diminishing the geometric deviation from the base material, the first group focusses on prevention of stress concentrations. Modifying the RS states in the weld proximity, particularly reducing possible tensile RS, is characterized by the second group, where the high-frequency mechanical impact (HFMI) technique shows the most promising results. The third group focusses on improving environmental condition and shielding the weld off influential environments by means of coatings.[6–8]

Coatings can be used in an alternative way, that is by the introduction of RS in the near surface regions or suppression of persistent slip bands, the precursor of fatigue crack initiation sites:

Exemplary on polyimide substrates, where a drastic increase in lifetime can be observed.[9,10] Coatings of pure Cu or Cu/Ni multilayer with layer thicknesses far below 1 µm show, that decreasing the individual layer thickness results in a decrease of the density of surface intrusions and extrusions, instead cracks initiate at internal defects and grain boundaries. Using pure Cu as a substrate material, a Cu/Ni multilayer is electrodeposited on Cu samples and fatigue testing is conducted.[11,12] The crack initiation period is prolonged and fatigue testing stopped after 5×10^7 cycles with no failure. The suppression of dislocation movement to the free surface prevents fatigue crack nucleation for multilayer coated materials. Further, for nanoscale multilayers with other metal combinations, an increased fatigue performance and prolonged crack initiation phase has been reported, as a result of suppression of persistent slip bands.[13–15] Alternatively, via the application of thin films and their inherit RS states an improvement in fatigue performance can also be

N. Spalek, M. Rutner
Hamburg University of Technology
Institute for Metal and Composite Structures
Denickestraße 17, 21073 Hamburg, Germany
E-mail: niclas.spalek@tuhh.de

G. Abreu Faria, A. Davydok
Helmholtz-Zentrum hereon GmbH
Max-Planck-Straße 1, 21502 Geesthacht, Germany

The ORCID identification number(s) for the author(s) of this article can be found under https://doi.org/10.1002/adem.202502357.

DOI: 10.1002/adem.202502357

detected.[16–19] Substrate material in close proximity of the coating is influenced to show compressive RS, thus reducing the effective stress amplitude at the surface and transferring crack initiation sites from the surface into the material.

This article seeks to give new insights into the underlying effects of the novel postweld treatment in using a Cu/Ni multilayer coating deposited onto industry-standard welded steel joints to improve the fatigue strength.

Previous studies[20,21] presented, that an improvement of 300%–600% in service life, depending on the applied load, is observed in butt-welded steel plates. The nanometallic multilayers (NMM) postweld treatment has been developed from small-scale laboratory tests[22–24] to a scalable technology[21] by using electrodeposition, applicable for new and existing structures[20,25–29] as well as for metal 3D-printed structures.[30] For the first time, the NMMs effect of welded joints is investigated, especially in regard to the underlying principles of fatigue enhancement. The hypothesized mechanisms are expected to rely heavily on the introduction of residual compressive stresses into the steel substrate and thereby prolonging the crack initiation phase and inhibiting crack propagation. Herein, the origin of RS in electrodeposited multilayer and their relationship in increasing the fatigue strength of welded joints is investigated by measuring the RS states in the multilayer coating, their influence on the compressive RS states in the substrate and their combined effect on fatigue strength.

2. Experimental Section

2.1. Welded Steel Samples

For fatigue strength evaluation, S355 J2 mild steel dog-bone samples according to DIN 50 125 type E are fabricated.[31] Two steel plates are welded together by MAG welding, using Linde CORGON 18 (18% CO_2/82% Ar) shielding gas with a volume flow of 10 L min^{-1}. The welding is performed by a UR10e welding robot, carrying a LORCH 5 XT using Böhler SG2 filler material. In **Table 1** the chemical composition of the substrate and filler material is shown. Using a double-V (DV) butt-weld, the plates are welded together. For the top and bottom V-weld, $I = 175$ & 205 A weld current and 7 & 11 mm sec^{-1} feed speeds are selected, respectively. The samples are dimensioned by waterjet cutting to the final measurements of 284×8 mm^2 (L × T) with 35 mm width in the grip section, thinned to 25 mm for the parallel width. A schematically depiction is shown in **Figure 1**a. Test pieces, that undergo polishing are abrasively grinded by up to 180 grit in parallel direction of the length. That way, scales and oxides are removed for further electrodeposition or testing.

Tensile testing of dog-bone samples showed a yield stress of $f_y = 370$ MPa, which is used to assess the stress amplitudes for subsequent cyclic loading. Tensile-tensile fatigue testing is performed and evaluated according to DIN 50 100[32] on a servo-hydraulic uniaxial testing machine (Schenck PC400M) with a frequency of $f = 8$ Hz. During testing the σ_{max} is set to the described percentage of yield strength, while σ_{min} is set to zero, resulting in a stress ratio $R = 0$. Test piece failure occurs with complete rupture. Run-outs are considered, when cycle numbers exceed $N_f = 2.5 \times 10^6$ cycles, and are not included in calculation of the S-N curves.

The S-N curves of the polished weld and parameter set D are taken from Brunow et al.[20] Parameter sets A–C are tested on a fixed stress range, i.e., $\Delta\sigma_R = 0.75 \times f_y$.

2.2. NMM Deposition Process

Different layups of the nanometallic multilayer are selected for this study. It is investigated how the variation of layer characteristics changes the RS in the thin film and subsequently impacts the RS states in the steel adjacent to the surface, ultimately affecting the fatigue strength.

The NMM used herein is an electrodeposited thin film, composed of alternating Copper and Nickel nanolayers. A summary of the governing deposition parameters is given in **Table 2**.

As the influence of RS is explored, the respective sample conditions are selected to increase the magnitude of RS states. Increasing the current densities under which the thin film is produced, usually results in an increase in inherent RS.[33,34] The role of the Ni striking/leveling layer is increasing adhesion of the multilayer system on the steel based substrate. Reducing the leveling layer to a minimum, allows for an unhindered force transfer between the multilayer and the substrate, without a buffering interlayer in between. Lastly, the reduction of individual layer thicknesses is hypothesized to exhibit higher RS as a result of higher strength, following the effect of grain boundary strengthening. The standard layup is sample condition D, which has been used in a previous publication.[20] From this, the variants with higher current density (sample condition A), a thinner leveling layer (sample condition B), and halved layer thickness (sample condition C) are derived.

Before the electrodeposition process, oxides and scales are removed by polishing and the specimen are thoroughly cleaned by ultrasonic treatment. Electrodeposition with a citrate Cu/Ni sulfate-based electrolyte is performed in a single-bath configuration adopted from Bonhote et al.[35] Using a pulse power supply galvanostat (Plating Electronics pe86CB-20-5-25-SGD), the NMM is deposited up to a total thickness of $t_{total} = 9$ µm.

2.3. Materials Characterization

Herein, three approaches are followed: First, fatigue testing is conducted to examine the performance of the NMM postweld

Table 1. Chemical composition of base, according to material certificate and filler material.

Alloying element	C [wt%]	Mn [wt%]	Si [wt%]	Cu [wt%]	Cr [wt%]	P [wt%]	S [wt%]
S355 J2	0.12	1.33–1.36	0.19–0.24	0.23–0.3	0.7–0.17	≤0.018	≤0.025
SG2	0.07	1.5	0.85	0	0	0	0

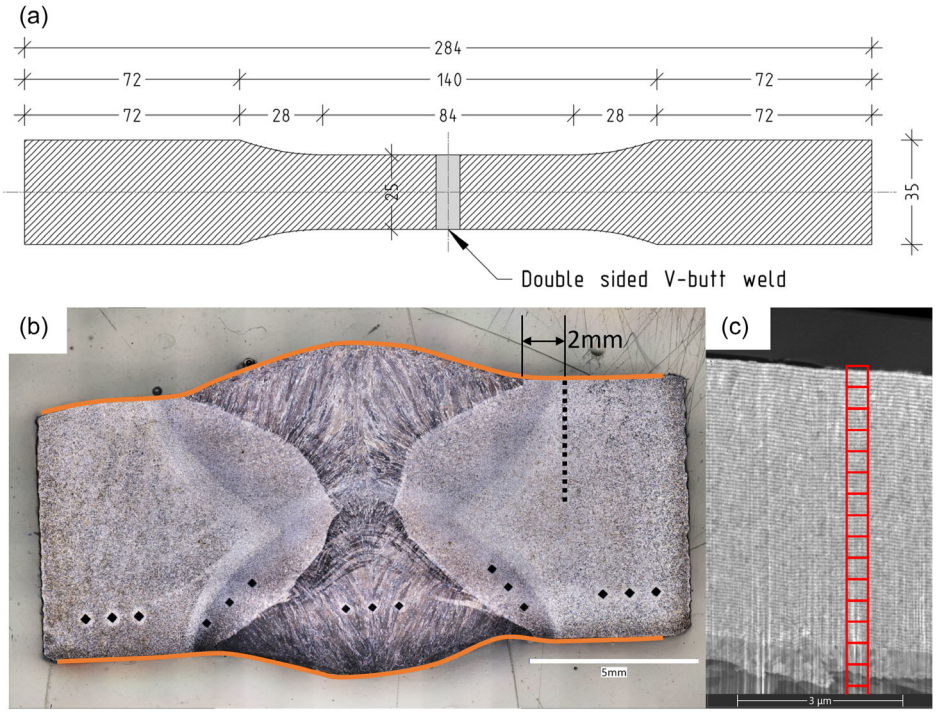

Figure 1. a) Schematic drawing of the dog-bone sample dimensions annotated in mm. b) Cross-sectional micrograph of a welded sample with the NMM highlighted in orange. EDXRD measurement is performed along dotted line to a total depth of 250 µm. c) SEM image of a NMM cross-section, where the individual Copper and Nickel layers are visible by different contrasts. Contrary to samples in this study, the image shows an exemplary sample with 5 µm total thickness. Red squares schematically show measurement areas for nanodiffraction measurements.

Table 2. Deposition parameters for all sample sets.

Sample	A	B	C	D
Total NMM thickness [nm]	9000	9000	9000	9000
Nickel leveling layer thickness [nm]	1000	100	1000	1000
Copper layer thickness [nm]	15	15	7,5	15
Nickel layer thickness [nm]	35	35	17,5	35
Copper current density [mA cm^{-2}]	0.8	0.8	0.8	0.45
Nickel current density [mA cm^{-2}]	50	50	50	22

treatment. Second, the fatigue data is correlated with the evolution of the RS in the steel substrate using energy dispersive X-ray strain analysis. Lastly, nanodiffraction experiments are performed to explain the RS development in the steel depending on the deposited NMM layup, thus providing an approach to tune the fatigue strength increase which corresponds to lifetime extension of metal infrastructure. A polished and etched cross-section image of the weld, HAZ and base material is shown in Figure 1b. The NMM covers weld, HAZ, and partially base material. The multilayer thickness, layup configuration, and individual layers are characterized using a DualBeam focused ion beam/scanning electron microscopy (FIB/SEM) FEM Helios Nanolab G3. A rectangular trench is milled by means of FIB and examined by SEM.

In order to measure RS distribution in the NMM as well as in the steel substrate, different approaches are taken:

2.3.1. Energy Dispersive X-Ray Diffraction Strain Analysis

Energy dispersive X-ray diffraction (EDXRD) is carried out at the white-beam beamline P61A of PETRA-III at DESY, Hamburg. The polychromatic, high incident spectrum of $E = 30$–200 keV enables penetration through the entire specimen along the 25 mm width of the specimen and receiving sufficient diffraction data in a timely fashion. The beamline is equipped with two independently positioned point detectors at $2\theta_0 = 5.815°$ vertically and $2\theta_1 = 4,488°$ horizontally. The collimator slits are set to guarantee a 10 µm measurement height, i.e., each data point represents a 10 µm step along the cross-section.

A total of 25 measurements are taken for each sample, thereby getting diffraction data up to 250 µm cross-sectional depth. The samples are oriented so that the gauge volume is always centered on the specimen, thereby preventing partially filled gauge volumes. The measurements are performed in transmission mode. The experimental setup is shown in **Figure 2**a, with the beam and its diffracted path to the horizontal and vertical detectors. Peak fitting is conducted with in-house software P61Viewer using the Pseudo-Voigt fitting method. All strain analysis is performed on the (211) reflection. For the calculation of strains in an energy dispersive experiment, Bragg's law takes the form of

$$d(hkl) = \frac{hc}{2\sin\theta_d}\frac{1}{E(hkl)} = \text{const}\frac{1}{E(hkl)} \quad (1)$$

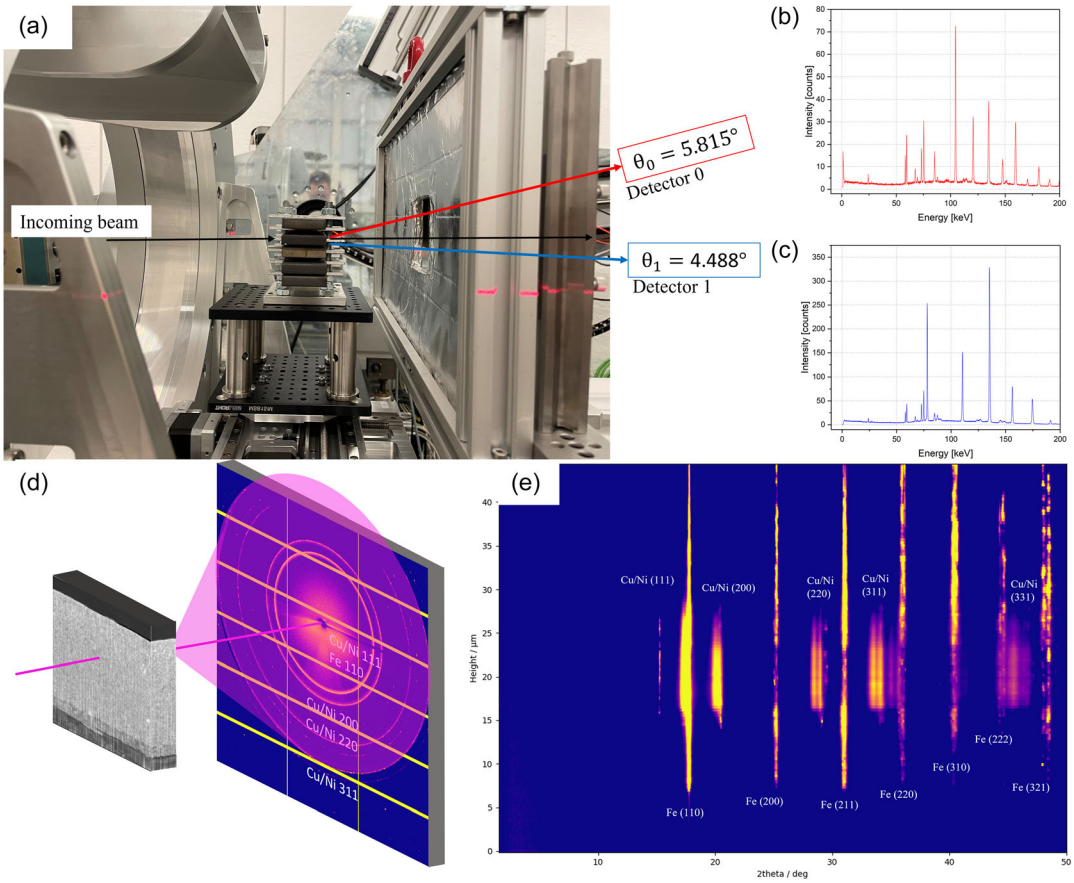

Figure 2. a) EDXRD experimental setup with the incoming beam, the sample holder, and the diffracted beams reaching the point detectors. b) Energy dispersive intensity spectrum acquired by detector 0 at $2\theta_0 = 5.815°$. c) Energy dispersive intensity spectrum acquired by detector 1 at $2\theta_1 = 4.488°$. d) Schematic depiction of the P03 experiment with the incoming beam, the sample, and a DS-ring, diffracted onto the detector. e) Radial integration of sample A with the crystallographic planes denoted. Square root of the counts is taken to increase visibility of planes with different intensities. Integration and data analysis are performed with hereon in-house software Pydidas.[32]

h is Planck's constant, c the velocity of light, θ_d the diffraction angle, and $E(hkl)$ the corresponding energy satisfying Bragg's law. Thereby the lattice strain is calculated

$$\varepsilon_{\varphi\psi}(hkl) = \frac{d(hkl) - d_0(hkl)}{d_0(hkl)} = \frac{E_0(hkl)}{E_{\varphi\psi}(hkl)} - 1 \tag{2}$$

where subscript 0 refers to the stress-free lattice plane distance or energy, respectively.[36] The experiment is set up, that the strains are in principle directions, setting the shear strain components to zero. Simultaneously, the out-of-plane strains cannot be measured in this test configuration and are also ignored herein. With $\sigma_{22} = \sigma_{12} = \sigma_{13} = \sigma_{23} = 0$, the fundamental equation of X-ray stress analysis (XSA) becomes

$$\varepsilon_{11}(hkl) = \frac{1}{2} s_2 \sigma_{11} + s_1(\sigma_{11} + \sigma_{33}) \tag{3}$$

$$\varepsilon_{33}(hkl) = \frac{1}{2} s_2 \sigma_{33} + s_1(\sigma_{11} + \sigma_{33}) \tag{4}$$

Measurements are taken ≈2 mm from the weld toe to lie in the HAZ, to get accurate information about the change in RS by the NMM, including the influences of phase transformation and subsequent lattice expansion.

2.3.2. X-ray Nanodiffraction Strain Analysis

For investigating the RS development within the NMM, nanodiffraction experiments at the P03 micro and nanofocus small- and wide-angle X-ray scattering beamline (MiNaXS) at PETRA-III (denoted as P03 experiment) at DESY, Hamburg are performed. Because of the comparable low photon energy of $E = 19.8$ keV, special sample preparation is necessary. Rapid X-ray attenuation within Ni and Cu necessitates the use of thin lamellae. They are produced by precision sawing (Buehler IsoMet 4000) from the dog-bone test pieces used in the fatigue experiment. The dimensions after cutting are 20×8 mm^2 (W × H) with a thickness of $t = 200$–300 µm. With further decrease in thickness, bending, and stress relaxation occurs, which impacts the validity of the experiment. The experimental setup is shown in Figure 2d, where the beam is scanned across the height and the diffracted Debye-Scherrer (DS)-rings are detected. The beam is focused by KB-mirrors to a small field of 350×250 nm^2 (H × W), then

transmitted through the sample. After diffraction, the signal is detected by means of single counting detector Dectris EIGER 9 M, where DS-rings can be analyzed. The sample-detector distance is fixed to $d_{\mathrm{det}} = 17$ cm, which allows the analysis of DS-rings up to $2\theta \approx 45°$. The depth scan starts at the sample surface and reaches a total depth of 45 µm with a step size of 0.35 µm. RS analysis is performed by means of the $\sin^2\psi$ method. Because of the position of the beam-center on the detector, only the bottom half of the DS-ring can be used for analysis. The half-circle is divided into 19 sections, each section with an azimuth angle segment of $\delta \pm 5°$, then azimuthally integrated and peak fitted. The corresponding $d_{\delta\theta}(hkl)$ are calculated by standard Bragg's Law. The $d_{\delta\theta}(hkl)$ versus $\sin^2\psi$ plots are linearly fitted. Following

$$\sigma_{11} = \frac{1}{d_0}\frac{1}{\frac{1}{2}s_2}\frac{\partial d_{\theta\delta}}{\partial \sin^2\psi} \tag{5}$$

the RS can be calculated with the respective $d_0(hkl)$ and X-ray elastic constants (XEC) values for Cu and Ni, taken from the software IsoDEC.[37] $\sigma_{33} = \sigma_{12} = \sigma_{13} = \sigma_{23} = 0$ is applied.[38] In order to investigate the RS states of the sample, the data is processed with Hereon in-house software Pydidas.[39] For all diffraction data, careful selection of the desired DS-rings for analysis is required as Cu and Ni peaks are overlapping. A fully integrated detector image is shown in Figure 2e. The respective crystallographic planes are denoted as well. Selecting a peak for strain analysis has to fulfill four requirements: First, no superposition between the Fe and neither Cu nor Ni peaks should be visible. Second, the respective Cu and Ni peaks should not overlap to yield peak identification and fitting to satisfactory results. Third, intensity of the selected peaks should be sufficient for subsequent peak fitting and data analysis. Lastly, intersection of the strain models poses an additional constraint. For the given *hkl*, the Reuss, Eshelby-Kröner, and Voigt models should intersect, allowing for valid predictions for strain evaluation of the entire polycrystalline material.[40] As a result, for Copper and Nickel the (311) plane is selected.

The purpose of the experiment at beamline P03 is to investigate the RS states in the NMM. Although measurements are also taken of the steel substrate beneath, the primary focus of this analysis is on the NMM, which is anticipated to exhibit an equibiaxial stress state predominantly defined by the process parameters. In contrast, the steel substrate is influenced by the broader manufacturing and preparation processes. Extrapolating results from the nanoscale test volume, measuring $0.35 \times 0.25 \times 300\ \mu m^3$ (H × W × T), to the entire steel substrate is not feasible. Furthermore, variations in experimental outcomes can be partly attributed to the smaller gauge volume used in the P03 experiment. This limitation hampers the statistical reliability of results due to the reduced number of diffracting grains compared to experiments with larger gauge volumes. However, this issue is less pronounced for the Cu/Ni multilayer, as the nanoscale dimensions of individual grains result in a larger number of diffracting grains within the gauge volume, thereby enhancing the statistical robustness of the measurements. As illustrated in Figure 2e, the diffraction data reveals information from different planes and elements. The simultaneous measurement of the ferrite, alongside the Cu/Ni phases suggests potential misalignment, however, it is more plausible that the surface roughness exceeds the coating height of $t_{\mathrm{total}} = 9$ µm. Additionally, it is important to note, that the incoming beam has a focus point, where the dimensions $350 \times 250\ nm^2$ hold true. Beyond this focal point, the beam experiences slight divergence, which could influence the accuracy of the measurements.

3. Results and Discussion

Table 3 summarizes fatigue test results. While the S-N curves include a wide array of tested stresses, sample sets A–C are tested at a fixed stress range of $\Delta\sigma_R = 0.75 \times f_y$, the individual sample results are presented. The table presents mean fatigue life values $N_{f,M}$ for each parameter set, with all samples included, except the run-outs. Mean cycles to failure for sample set D, polished and as-welded are deducted from the $\Delta\sigma_{R,50\%}$ S-N curves intersection with $\Delta\sigma_R = 0.75 \times f_y$. **Figure 3**a presents mean S-N curves $\Delta\sigma_{R,50\%}$ for DV butt-welded specimens in three conditions: as-welded, as-welded + polished, and after nanometallic multilayer postweld treatment, compared with data from recent studies.[20] Fatigue data points for sample sets A–C, tested at maximum stress level $\Delta\sigma_R = 0.75 \times f_y$, are indicated in the Figure 3. The relative probability distribution is depicted as a normal distribution in the accompanying rug plot below. The NMM postweld treatment significantly enhances fatigue strength compared to both as-welded and polished conditions. Sample set D shows a pronounced reduction in S-N curve slope to $m = 6.3$. As detailed in Table 2, the sample sets vary in deposition parameters. All parameter combinations increase fatigue strength compared to the as-welded + polished condition. Among sample sets A–C, condition B demonstrates the most notable improvement, achieving a mean cycles-to-failure $N_{f,M} = 431823$ cycles, representing a 16.5% enhancement in service life at the tested stress level, compared to previously published sample set D from Brunow et al.[20] That amounts to an absolute increase in mean cycles-to-failure $N_{f,M}$ of 309% compared to the as-welded sample set. Conversely, sample set C yields a lower fatigue strength improvements compared with sample set D, while sample set A exhibits only slight decrease in performance. With sample sets D, polished and as-welded the endurance limit can be presumed. For as-welded samples, the endurance limit seems to be located around $S_{f,\text{as-welded}} = 0.3 \times f_y$, for polished samples $S_{f,\text{polished}} = 0.6 \times f_y$ and for NMM coated samples the endurance limit is presumed to be $S_{f,\text{NMM}} = 0.7 \times f_y$. These preliminary findings require confirmation through additional testing. For all samples, extrapolated mean S-N curves are also included to visualize the change in the respective slopes. With sample set B, the slope is further reduced to $m = 6.6$. In the rug plot of Figure 3a, the normal distributions of the experimental data are shown. For each of the data points of sample set A–C the relative probability is plotted against the respective cycles to failure N_f.

RS measurements are conducted at beamline P61A to investigate NMM effects on the steel substrate and correlate findings to the fatigue test data. The high-energy white-beam beamline enables penetration of thick samples without pretreatment, that could alter RS states. Stress-free lattice parameters are obtained by annealing, followed by analysis using lab-XRD (Stresstech Xstress DR45). The strain-free lattice spacing is determined as $d_{0,\mathrm{Fe}} = 0.28680157$ nm. This study provides the first

Table 3. Cycles to failure for all sample sets. Mean cycles to failure for sample sets A–C is calculated from the cycles to failure N_f, tested at $\Delta\sigma_R = 0.75 \times f_y$, presented herein. Sample set mean values for D, polished, and as-welded are derived from the S-N curves intersection with the stress level $\Delta\sigma_R = 0.75 \times f_y \triangleq$ 277.5 MPa.

Sample set	A	B	C	D	Polished	As-welded
	648 581	442 884	228 959		Data points taken from ref. [20]	
	1 429 840	379 458	342 377	–	–	–
	114 822	361 609	436 878	–	–	–
	81 207	275 566	134 397	–	–	–
	69 315	1 193 901	221 371	–	–	–
	707 967	254 173	203 608	–	–	–
	80 985	292 820	233 510	–	–	–
	171 321	254 173	–	–	–	–
	29 079	–	–	–	–	–
	198 293	–	–	–	–	–
	214 440	–	–	–	–	–
	335 265	–	–	–	–	–
	300 825	–	–	–	–	–
	139 960	–	–	–	–	–
Mean cycles to failure $N_{f,M}$ [–]	322.992	431.823	257.300	370.710	178.064	140.737

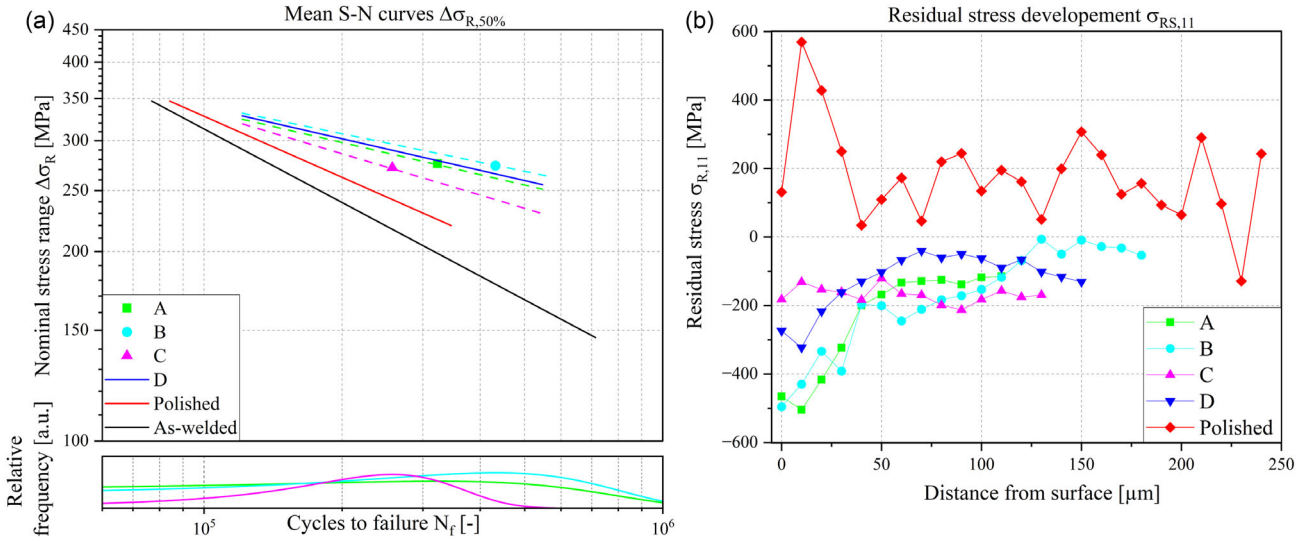

Figure 3. a) Mean S-N curves for samples in the as-welded condition, after surface polishing, and after subsequent NMM postweld treatment. Data points represent sample sets A–C tested at a stress range of $\Delta\sigma_R = 0.75 \times f_y$. Dotted lines indicate extrapolated mean S-N curves based on experimental data points. The rug plot represents the normal distribution of the experimental data for the respective sample sets A–C. b) RS $\sigma_{RS,11}$ in the steel substrate for the in-plane s11 direction across the depth profile. For RS evaluation, the Fe (211) planes are evaluated.

comprehensive analysis of absolute RS values and distributions within both substrate and NMM layers. Sample D from previous work[20] is included for comparison, with electroplating current densities of 0.45 and 22 mA cm^{-2} for Copper and Nickel, respectively.

Figure 3b presents RS distributions versus specimen depth. Consistently high compressive RS are observed in the steel substrate, with absolute values exceeding the yield strength of base steel S355. This phenomenon is attributed to surface preparation[41] and 3D compressive stress states created by the NMM and surrounding material, which inhibit dislocation movement. In contrast, polishing produces tensile RS, with peak stress $\sigma_{RS,11} = 570$ MPa near the surface, equivalent to the steel ultimate tensile strength.

RS measurements reveal that all NMM-treated specimens exhibit beneficial compressive RS in the steel substrate caused

by tensile RS in the NMM. Sample A demonstrates compressive stresses extending throughout the measured depth profile, with maximum compressive stress reaching $\sigma_{RS,11} = -504$ MPa at the substrate-coating interface. The fundamental distinction between samples A and D is attributed to variations in electrodeposition current density, a processing parameter that significantly influences mechanical properties, including hardness and RS distribution.[42,43]

Sample B, characterized by a reduced nickel leveling layer thickness of $t_{Ni} = 100$ nm, exhibits high compressive RS of $\sigma_{RS,11} = -496$ MPa, which correlate directly with enhanced fatigue performance. In contrast, Sample C, featuring halved individual layer thickness, displays the lowest compressive RS of $\sigma_{RS,11} = -211$ MPa, despite maintaining relatively uniform stress distribution across the measured depth. Sample D, retains substantial compressive stresses $\sigma_{RS,11} = -325$ MPa following fatigue testing, demonstrating the durability and robustness of the treatment under cyclic loading.

The occurrence of residual tensile stresses in the NMM during processing which cause residual compressive stresses in the steel substrate is seen as a central mechanism for fatigue life enhancement. These residual compressive stresses in the substrate effectively mitigate localized stress concentrations. A key advantage of NMM treatment lies in its comprehensive 2D surface coverage, which addresses all potential failure initiation sites including surface extrusions, material defects, pre-existing cracks, and geometric notches across the treated surface. The comprehensive nature of NMM surface modification provides superior reliability and treatment consistency compared to 1D postweld improvement techniques such as HFMI, as previously shown in Brunow et al.[20]

Figure 4 presents RS measurements for samples A–C following the $\sin^2\psi$ method. All samples exhibit residual tensile stresses, consistent with literature findings.[44–46] Nickel consistently exhibits higher residual tensile stresses relative to Copper, with approximately constant stress distributions across the $t_{total} = 8$ µm multilayer depth.

Sample A, characterized by individual layer thicknesses of $t_{Cu,ind} = 15$ nm and $t_{Ni,ind} = 35$ nm, demonstrates maximum stresses of $\sigma_{RS,Ni} = 1.08$ GPa and $\sigma_{RS,Cu} = 376$ MPa. The measured Nickel stress exceeds the yield strength of monolithic hot-rolled Nickel,[47] which is attributed to grain size refinement resulting from reduced layer thickness and subsequent grain boundary strengthening consistent with the Hall-Petch relationship.[48] Nickel yield stresses exceeding $\sigma_{y,Ni} > 2$ GPa have been reported in nanocrystalline systems,[49] therefore RS above 1 GPa in Nickel are considered reasonable. Although Copper generates RS through similar mechanisms, measured magnitudes remain substantially lower. Nickel emerges as the primary contributor to residual tensile stress development, evidenced by both superior absolute stress values and greater volumetric fraction.

Sample B maintains identical individual layer thicknesses of $t_{Cu,ind} = 15$ nm and $t_{Ni,ind} = 35$ nm but has a reduced leveling layer thickness of $t_{Ni} = 100$ nm—one-tenth that of sample A. Sample B shows the highest fatigue strength improvement and prominent residual compressive stress distribution in the steel substrate with maximum stress exceeding the steels axial yield strength at $\sigma_{RS,Ni} = 658$ MPa, as demonstrated in Figure 3b, P03 experiment results reveal significantly lower residual tensile stresses in the NMM Copper and Nickel layers compared to sample A. The RS values from sample B are derived from a slightly different experimental setup. All samples are measured with the beam size set to nanobeam size, i.e., 350×250 nm^2. Additionally, microbeam measurements are conducted with a beam size of 1×1 µm^2. During the measurement of sample B, the synchrotron facility experienced a beam drop, where no nanobeam diffraction data for sample B was collected. Therefore, the microbeam plot is presented. The findings shown in Figure 4 confirm tensile RS within the multilayer system.

Sample C employs reduced individual layer thicknesses of $t_{Cu,ind} = 7.5$ nm and $t_{Ni,ind} = 17.5$ nm, which is half the individual layer thicknesses of samples A and B. The steel substrate exhibits reduced residual compressive stress of approximately $\sigma_{RS,Fe} = -200$ MPa, correlating with reduced fatigue strength improvement compared to sample B.

RS measurements in sample set C, NMM confirm tensile stress states distributed uniformly across the multilayer cross-section. Maximum tensile stresses reach $\sigma_{RS,Ni} = 811$ MPa and $\sigma_{RS,Cu} = 177$ MPa for Nickel and Copper layers, respectively.

Tensile RS in electrodeposited multilayers originate from several mechanisms during film growth. Atomic incorporation processes, lattice parameter mismatches between dissimilar materials, grain coalescence events, and constrained thermal expansion collectively generate internal stress fields.[42,44,50,51] Additionally, the electrodeposition process inherently introduces crystallographic defects and high-angle grain boundaries that

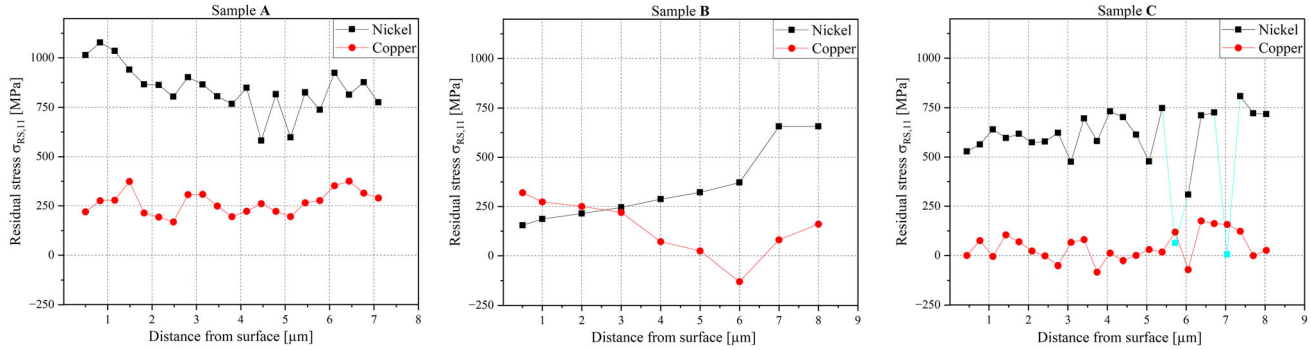

Figure 4. RS in the NMM for the in-plane biaxial s11/s22 direction. For RS evaluation, the Ni (311) and Cu (311) planes are selected for samples A, B, and C. Data analysis is performed with DESY in-house software Pydidas,[32] following the $\sin^2\psi$ method. Erroneous data points due to peak misfit are cyan colored.

contribute to stress accumulation. The mechanical properties and consequent RS evolution can be fine-tuned through careful control of the ionic concentrations, the use of specific additives in the plating bath, and optimization of processing parameters. Among these, current density stands out as the principal parameter governing mechanical properties during deposition. Elevated current densities enhance the nucleation rate of crystallites, leading to grain refinement and an associated increase in material strength.[42,44,50–56]

The substantial residual compressive stresses in the substrate correlate with significant fatigue strength improvements as seen in Figure 3. Sample C, despite utilizing identical current density as samples A and B, exhibits reduced residual compressive stress in the steel substrate, suggesting that reduced individual layer thickness, particularly Nickel, yields to lower induced RS states and correspondingly reduced fatigue strength enhancement in comparison to previously published findings.[20]

Sample D, processed at lower current density, demonstrates significant residual compressive stress and high fatigue strength improvement to a FAT class 181. This indicates that beyond current density, individual layer thickness, particularly of Nickel, critically influences fatigue performance. Additional parametric studies are required to fully understand the governing process parameters responsible for residual compressive stress built-up in the substrate and corresponding fatigue strength increase.

Residual tensile stresses in the NMM serve as the primary mechanism generating substrate compressive stresses, thereby suppressing crack initiation and propagation while enhancing fatigue strength. However, secondary effects including increased NMM hardness may also contribute to fatigue improvement and service life extension observed in all NMM-treated welds.

4. Conclusion

Herein a novel postweld treatment, employing NMM is investigated with particular emphasis on the RS states induced during the deposition process. Tensile RS are inherently created during the deposition within the NMM, which induce residual compressive stress states in the underlying steel substrate by stress equilibration. Acting as a 2D surface treatment, the NMM effectively covers and mitigates surface-related weaknesses, which is identified as crucial in driving the significant improvements in fatigue strength. The multiscale approach combines the investigation of RS development within the NMM and its effect on the steel substrate to explain the fatigue strength increase. The conclusions drawn from this study can be summarized as follows: 1) Across all samples, nanodiffraction data shows that tensile RS are inherently created during the deposition process in the NMM. 2) A correlation emerges between the development of compressive RS in treated welds and fatigue strength increase compared to as-welded samples. 3) With a thinner leveling layer (100 vs. 1000 nm) the resulting cycles to failure are further increased, presumably by better transition of stresses into the substrate. 4) Nickel is identified as the primary constituent of the multilayer, responsible for introduction of RS in the thin film, with its increased absolute RS values and its higher volumetric fraction.

These findings demonstrate that careful tuning of process parameters offers a versatile toolkit for tailoring RS profiles, thereby enabling controlled enhancements in fatigue performance and service life extension of welded steel components. Future work will focus on further investigating the role of RS in the coating, their influence into the substrate and the effect of fatigue, summarized in S-N curves. Additionally, the role of material properties, such as hardness, ductility, and roughness are to be investigated.

Acknowledgements

The authors acknowledge DESY, Hamburg, a member of the Helmholtz Association HGF, for positively evaluating the proposal I-20230348 and I-20230354, with special thanks to Dr. Abreu Faria and Dr. Davydok in their assistance as the beamline scientists at P61A and P03, respectively. Publishing fees are supported by Funding Program Open Access Publishing of Hamburg University of Technology.

Open Access funding enabled and organized by Projekt DEAL.

Conflict of Interest

The authors declare no conflict of interest

Data Availability Statement

The data that support the findings of this study are available from the corresponding author upon reasonable request.

Keywords

electrodeposition, fatigue, infrastructure, lifetime extension, nanometallic multilayer, postweld treatment, thin films

Received: September 10, 2025
Revised: October 29, 2025
Published online:

[1] D. R. Cooper, A. C. H. Skelton, M. C. Moynihan, J. M. Allwood, *Resour. Conserv. Recycl.* **2014**, *84*, 24.
[2] L. Aucott, D. Huang, H. B. Dong, S. W. Wen, J. A. Marsden, A. Rack, A. C. F. Cocks, *Sci. Rep.* **2017**, *7*, 40255.
[3] G. Totten, *Handbook of Residual Stress and Deformation of Steel*, ASM International, Materials Park, Ohio **2008**.
[4] J. Hensel, T. Nitschke-Pagel, K. Dilger, *Weld World* **2015**, *59*, 179.
[5] V. Chmelko, M. Margetin, M. Harakal, *MATEC Web Conf.* **2018**, *165*, 21003.
[6] A. Hobbacher, *Recommendations for Fatigue Design of Welded Joints and Components*, Springer International Publishing, Cham; Heidelberg; New York; Dordrecht; London **2018**.
[7] *IIW Recommendations for the HFMI Treatment: For Improving the Fatigue Strength of Welded Joints* (Ed: B. Marquis), Springer, Singapore **2016**.
[8] P. J. Haagensen, S. J. Maddox, *IIW Recommendations on Methods for Improving the Fatigue Strength of Welded Joints: IIW-2142-10*, Woodhead Publ.; International Institute Of Welding, Cambridge, UK; Philadelphia, PA **2013**.
[9] D. Wang, C. A. Volkert, O. Kraft, *Mater. Sci. Eng.: A* **2008**, *493*, 267.
[10] X. F. Zhu, G. P. Zhang, *J. Phys. D: Appl. Phys.* **2009**, *42*, 055411.

[11] M. R. Stoudt, R. E. Ricker, R. C. Cammarata, *Int. J. Fatigue* **2001**, *23*, 215.
[12] Y. Kaneko, Y. Nishijima, T. Sanda, S. Hashimoto, *MSF* **2007**, *561–565*, 2393.
[13] Y.-C. Wang, A. Misra, R. G. Hoagland, *Scr. Mater.* **2006**, *54*, 1593.
[14] D. Wang, P. A. Gruber, C. A. Volkert, O. Kraft, *Mater. Sci. Eng.: A* **2014**, *610*, 33.
[15] S. Wei, Z. Zhao, S. Zheng, H. Wei, J. Wang, *Scr. Mater.* **2021**, *190*, 103.
[16] S. Baragetti, *Open Corros. J.* **2011**, *4*, 9.
[17] Y. Zhou, G. B. Rao, J. Q. Wang, B. Zhang, Z. M. Yu, W. Ke, E. H. Han, *Thin Solid Films* **2011**, *519*, 2207.
[18] A. Gitschthaler, R. Hahn, L. Zauner, T. Wojcik, F. Fahrnberger, H. Hutter, A. Davydok, C. Krywka, C. Jerg, J. Ramm, A. Eriksson, S. Kolozsvári, P. Polcik, H. Riedl, Enhancing the High-Cycle Fatigue Strength of Ti-Al-N Coated Ti-6al-4v by Residual Stress Design **2025**.
[19] J. A. M. De Camargo, H. J. Cornelis, V. M. O. H. Cioffi, M. Y. P. Costa, *Surf. Coat. Technol.* **2007**, *201*, 9448.
[20] J. Brunow, N. Spalek, F. Mohammadi, M. Rutner, *Sci. Rep.* **2023**, *13*, 22215.
[21] J. Brunow, S. Gries, T. Krekeler, M. Rutner, *Scr. Mater.* **2022**, *212*, 114501.
[22] J. Brunow, M. Rutner, *Stahlbau* **2021**, *90*, 691.
[23] M. G. Ramezani, M. J. Demkowicz, G. Feng, M. P. Rutner, *Scr. Mater.* **2017**, *139*, 114.
[24] J. Brunow, M. Ritter, T. Krekeler, M. Ramezani, M. Rutner, *Scr. Mater.* **2021**, *194*, 113687.
[25] M. Rutner, N. Lalkovski, M. Falah, M. Seidelmann, N. Spalek, *Struct. Integr. Procedia* **2025**, 67.
[26] M. Seidelmann, N. Spalek, M. Falah, N. Lalkovski, M. Rutner, *Structural Integr. Procedia* **2025**, 67.
[27] M. Rutner, N. Spalek, M. Falah, N. Lalkovski, *Stahlbau* **2024**, *93*, 584.
[28] N. Spalek, J. Stührenberg, A. Tandon, M. Tourneau, A. Patel, B. Große, Robot-Based Installation of Nanostructured Metal Multilayers on Civil Infrastructure **2024**.
[29] N. Spalek, M. Falah, M. Seidelmann, N. Lalkovski, G. Abreu-Faria, M. Rutner, *Structural Integr. Procedia* **2025**, 67.
[30] M. Falah, R. Lau, N. Spalek, N. Lalkovski, M. Rutner, *Struct. Integr. Procedia* **2025**, 67.
[31] DIN 50125:2022-08: *Prüfung Metallischer Werkstoffe - Zugproben*, Beuth Verlag GmbH, Berlin **2022**.
[32] DIN 50100:2016-12: *Schwingfestigkeitsversuch - Durchführung Und Auswertung Von Zyklischen Versuchen Mit Konstanter Lastamplitude Für Metallische Werkstoffproben Und Bauteile*, Beuth Verlag GmbH, Berlin **2016**.
[33] Y. Kilinc, U. Unal, B. E. Alaca, *Microelectron. Eng.* **2015**, *134*, 60.
[34] J. K. Luo, M. Pritschow, A. J. Flewitt, S. M. Spearing, N. A. Fleck, W. I. Milne, *J. Electrochem. Soc.* **2006**, *153*, D155.
[35] C. Bonhôte, D. Landolt, *Electrochim. Acta* **1997**, *42*, 2407.
[36] C. Genzel, C. Stock, W. Reimers, *Mater. Sci. Eng.: A* **2004**, *372*, 28.
[37] T. Gnaeupel-Herold, IsoDEC: Software for Calculating Diffraction Elastic Constants **2016**.
[38] L. Spieß, G. Teichert, R. Schwarzer, H. Behnken, C. Genzel, *Moderne Röntgenbeugung: Röntgendiffraktometrie Für Materialwissenschaftler, Physiker Und Chemiker*, Springer Spektrum, Wiesbaden **2019**.
[39] M. Storm, G. Lotze, Pydidas - Python Diffraction Data Analysis Suite, **2025**.
[40] V. Hauk, H. Behnken, *Structural And Residual Stress Analysis By Nondestructive Methods: Evaluation - Application - Assessment*, Elsevier, Amsterdam **2006**.
[41] W. Ding, L. Zhang, Z. Li, Y. Zhu, H. Su, J. Xu, *Int. J. Adv. Manuf. Technol.* **2017**, *88*, 2939.
[42] A. M. Engwall, Z. Rao, E. Chason, *Mater. Des.* **2016**, *110*, 616.
[43] F. Ebrahimi, Z. Ahmed, *J. Appl. Electrochem.* **2003**, *33*, 733.
[44] E. Chason, A. Engwall, F. Pei, M. Lafouresse, U. Bertocci, G. Stafford, J. A. Murphy, C. Lenihan, D. N. Buckley, *J. Electrochem. Soc.* **2013**, *160*, 3285.
[45] I. G. McDonald, W. M. Moehlenkamp, D. Arola, J. Wang, *Exp. Mech.* **2019**, *59*, 111.
[46] S. E. Hadian, D. R. Gabe, *Surf. Coat. Technol.* **1999**, *122*, 118.
[47] W.F. Gale, *Smithells Metals Reference Book*, Butterworth-Heinemann **2004**.
[48] E. O. Hall, *Proc. Phys. Soc. B* **1951**, *64*, 747.
[49] R. W. Armstrong, *Philos. Mag.* **2016**, *96*, 3097.
[50] B. M. Clemens, H. Kung, S. A. Barnett, *MRS Bull.* **1999**, *24*, 20.
[51] A. R. Shugurov, A. V. Panin, *Tech. Phys.* **2020**, *65*, 1881.
[52] J. Yang, P. Ji, J. Zhang, W. Xu, J. Jiao, Y. Lian, L. Jiang, B. Zhang, *Surf. Coat. Technol.* **2023**, *471*, 129868.
[53] A. Bachmaier, H. Krenn, P. Knoll, H. Aboulfadl, R. Pippan, *J. Alloys Compd.* **2017**, *725*, 744.
[54] M. Huff, *Micromachines* **2022**, *13*, 2084.
[55] G. Abadias, E. Chason, J. Keckes, M. Sebastiani, G. B. Thompson, E. Barthel, G. L. Doll, C. E. Murray, C. H. Stoessel, L. Martinu, *J. Vacuum Sci. Technol. A* **2018**, 36.
[56] E. Chason, B. W. Sheldon, L. B. Freund, J. A. Floro, S. J. Hearne, *Phys. Rev. Lett.* **2002**, *88*, 156103.